A&A 619, A66 (2018)
https://doi.org/10.1051/0004-6361/201833847

Astronomy & Astrophysics

GRB 171205A/SN 2017iuk: A local low-luminosity gamma-ray burst

V. D'Elia[1], S. Campana[2], A. D'Aì[3], M. De Pasquale[4], S. W. K. Emery[5], D. D. Frederiks[6], A. Lien[7,8], A. Melandri[2], K. L. Page[9], R. L. C. Starling[9], D. N. Burrows[10], A. A. Breeveld[5], S. R. Oates[11], P. T. O'Brien[9], J. P. Osborne[9], M. H. Siegel[10], G. Tagliaferri[2], P. J. Brown[12], S. B. Cenko[13,14], D. S. Svinkin[6], A. Tohuvavohu[10], and A. E. Tsvetkova[6]

[1] Space Science Data Center - Agenzia Spaziale Italiana, via del Politecnico, s.n.c, 00133 Roma, Italy
e-mail: valerio.delia@asdc.asi.it
[2] INAF – Osservatorio Astronomico di Brera, via Bianchi 46, 23807 Merate, Italy
[3] INAF – IASF Palermo, via Ugo La Malfa, 153, 90146 Palermo, Italy
[4] Department of Astronomy and Space Sciences, Istanbul University, 34119 Beyazit, Istanbul, Turkey
[5] Mullard Space Science Laboratory, University College London, Holmbury St Mary, RH5 6NT Dorking, Surrey, UK
[6] Ioffe Physical-Technical Institute, Politekhnicheskaya 26, 194021 St. Petersburg, Russia
[7] Center for Research and Exploration in Space Science and Technology (CRESST), NASA Goddard Space Flight Center, 20771 Greenbelt, MD, USA
[8] Department of Physics, University of Maryland, 1000 Hilltop Circle, 21250 Baltimore County, Baltimore, MD, USA
[9] Department of Physics and Astronomy, University of Leicester, University Road, LE7 1RH Leicester, UK
[10] Department of Astronomy & Astrophysics, The Pennsylvania State University, University Park, 16802, PA, USA
[11] Department of Physics, University of Warwick, CV4 7AL Coventry, UK
[12] George P. and Cynthia Woods Mitchell Institute for Fundamental Physics & Astronomy, Texas A. & M. University, Department of Physics and Astronomy, 4242 TAMU, College Station, 77843, TX, USA
[13] Astrophysics Science Division, NASA Goddard Space Flight Center, Mail Code 661, 20771 Greenbelt, MD, USA
[14] Joint Space-Science Institute, University of Maryland, 20742 College Park, MD, USA

Received 13 July 2018 / Accepted 19 August 2018

ABSTRACT

Context. Gamma-ray bursts (GRBs) occurring in the local Universe constitute an interesting sub-class of the GRB family, since their luminosity is on average lower than that of their cosmological analogs. Attempts to understand in a global way this peculiar behaviour is still not possible, since the sample of low redshift GRBs is small, and the properties of individual objects are too different from each other. In addition, their closeness (and consequently high fluxes) make these sources ideal targets for extensive follow-up even with small telescopes, considering also that these GRBs are conclusively associated with supernova (SN) explosions.
Aims. We aim to contribute to the study of local bursts by reporting the case of GRB 171205A. This source was discovered by *Swift* Burst Alert Telescope (BAT) on 2017, December 5 and soon associated with a low redshift host galaxy ($z = 0.037$), and an emerging SN (SN 2017iuk).
Methods. We analyzed the full *Swift* dataset, comprising the UV-Optical Telescope (UVOT), X-ray Telescope (XRT) and BAT data. In addition, we employed the Konus-*Wind* high energy data as a valuable extension at γ-ray energies.
Results. The photometric SN signature is clearly visible in the UVOT u, b and v filters. The maximum emission is reached at ∼13 (rest frame) days, and the whole bump resembles that of SN 2006aj, but lower in magnitude and with a shift in time of +2 d. A prebump in the v-band is also clearly visible, and this is the first time that such a feature is not observed achromatically in GRB–SNe. Its physical origin cannot be easily explained. The X-ray spectrum shows an intrinsic Hydrogen column density $N_{\rm H,int} = 7.4^{+4.1}_{-3.6} \times 10^{20}$ cm^{-2}, which is at the low end of the $N_{\rm H,int}$, even considering just low redshift GRBs. The spectrum also features a thermal component, which is quite common in GRBs associated with SNe, but whose origin is still a matter of debate. Finally, the isotropic energy in the γ-ray band, $E_{\rm iso} = 2.18^{+0.63}_{-0.50} \times 10^{49}$ erg, is lower than those of cosmological GRBs. Combining this value with the peak energy in the same band, $E_{\rm p} = 125^{+141}_{-37}$ keV, implies that GRB 171205A is an outlier of the Amati relation, as are some other low redshift GRBs, and its emission mechanism should be different from that of canonical, farther away GRBs.

Key words. gamma-ray burst: general – gamma-ray burst: individual: GRB 171205A – supernovae: individual: SN 2017yup

1. Introduction

Long gamma-ray bursts (LGRBs) are the most powerful stellar explosions since the formation of the Universe. Most of their observed electromagnetic energy is released in the 0.01−1 MeV band, and they occur at a rate of one to two per day over the whole sky. Their subsequent fading emission, which is observed at multiple wavelengths, is long-lived and called the afterglow (see, e.g., Mészáros 2006 for a review), can outshine every other known object in the Universe, both in the optical/near-infrared (NIR) (e.g., Racusin et al. 2008) and in the X-rays (Cusumano et al. 2006). Contrary to their short-lived brothers, which last less than two seconds, LGRBs are thought to be the result of the core-collapse of a massive star, under the mechanism named the collapsar model (Woosley 1993; Paczynski 19998; MacFadyen & Woosley 1999). Alternatively, an exploding massive star in a binary system may cause the companion neutron star to reach the critical mass and to collapse into a black hole launching a GRB (Fryer et al. 2014). Given their extraordinary

power output at all wavelengths, LGRBs are detected up to very high redshifts (Tanvir et al. 2009; Salvaterra et al. 2009; Cucchiara et al. 2011), making them powerful probes of the early Universe (see, e.g., Vreeswijk et al. 2001; Berger et al. 2007; Fynbo et al. 2006a; Prochaska et al. 2007; Sparre & Starling 2012) .

Considering the other edge of the Universe, close-by LGRBs are equally important, because these sources show on average lower luminosities than cosmological events (e.g., GRB 980425 at $z = 0.0085$; Galama et al. 1998; Kulkarni et al. 1998; Pian et al. 2006; GRB 031203 at $z = 0.105$; Malesani et al. 2004; Soderberg et al. 2004; Watson et al. 2004; GRB 060218 at $z = 0.0331$; Campana et al. 2006; Mazzali et al. 2006a,b; Virgili et al. 2009; GRB 100316D at $z = 0.059$; Fan et al. 2011; Starling et al. 2011; Bufano et al. 2012), despite some noteworthy exceptions like GRB 130427A (Maselli et al. 2013). Both theoretical (e.g., Daigne & Mochkovitch 2007; Barniol Duran et al. 2015) and phenomenological (e.g., Virgili et al. 2009; Dereli et al. 2017) approaches have been attempted to explain the peculiarities of these sources in the framework of the standard GRB model. However, the sample is still sparse and the individual properties of these bursts are too different from each other to draw firm conclusions.

On the other hand, the connection between LGRBs and supernovae (SNe) is firmly established. This relationship can be directly probed only for low redshift events, as the SN emission becomes too faint to be detected at cosmological distances. In particular, for close-by events ($z < 0.3$), a detailed spectroscopic monitoring of the accompanying SN makes it possible to derive physical parameters of the ejecta and the progenitor (Galama et al. 1998; Patat et al. 2001; Hjorth et al. 2003; Stanek et al. 2003; Malesani et al. 2004; Pian et al. 2006; Bufano et al. 2012; Mazzali et al. 2006a,b; Woosley & Bloom 2006; Hjorth & Bloom 2012). These observations reveal that SNe accompanying LGRBs are explosions of bare stellar cores, that is, their progenitors (whose estimated mass is higher than $\sim 20\,M_{\odot}$) have lost all their hydrogen and helium envelopes before collapse (a.k.a. supernovae of type Ic). However, this scenario is challenged by two surprising exceptions: GRB 060505 at $z = 0.089$ and GRB 060614 at $z = 0.125$, which show no evidence for SN emission down to very deep limits, suggesting a new phenomenological type of massive stellar death (Della Valle et al. 2006; Fynbo et al. 2006b).

The GRB field was revolutionized by the *Neil Gehrels Swift* Observatory (Gehrels et al. 2004). After more than 13 years of operations, *Swift* has detected more than 1000 GRBs. The key to the success of this mission is its ability to quickly repoint its narrow field instruments and to obtain an arcsecond position of the afterglow in the X-ray and optical/UV bands within a few minutes. One of these bursts, GRB 171205A, was detected by *Swift* on 2017 December 5 and an association with a close-by galaxy at $z \sim 0.04$ was soon revealed (Izzo et al. 2017a). Given the proximity of this LGRB, the interest of the scientific community was testified by the massive follow-up of the afterglow at all wavelengths (see Sect. 4.1 for details).

In this work we have concentrated on the *Swift* data acquired for this special LGRB. The paper is organized as follows: Sect. 2 summarizes the properties of GRB 171205A and its association with a supernova, as reported in the literature; Sect. 3 introduces our dataset and illustrates the data reduction process, a subsection is devoted to each of the three *Swift* instruments; Sect. 4 presents and discusses our results; in Sect. 5 we draw our conclusions. Unless otherwise stated, we assume a cosmology with $H_0 = 67.3\,\mathrm{km\,s^{-1}\,Mpc^{-1}}$, $\Omega_\mathrm{m} = 0.315$, $\Omega_\Lambda = 0.685$ (Planck Collaboration XVI 2014).

2. GRB 171205A

GRB 171205A was discovered by the Burst Alert Telescope (BAT; Barthelmy et al. 2005) instrument on board *Swift* on 2017 December 5 at 07:20:43.9 UT (D'Elia et al. 2017). The BAT light curve shows some weak emission with multiple overlapping peaks that starts at $T_0 - 40$ s and ends at $T_0 + 200$ s, where T_0 is the burst detection time. The BAT spectrum is best fit by a simple power-law model (Barthelmy et al. 2017). The GRB was also detected by Konus-*Wind* (Frederiks et al. 2017). The X-Ray Telescope (XRT; Burrows et al. 2005) began observation the GRB about 150 s after the trigger (Kennea et al. 2017).

The Ultraviolet and Optical Telescope (UVOT, Roming et al. 2005) began settled observations of the field of GRB 171205A 154 s after the BAT trigger. A source consistent with the XRT enhanced position (Osborne et al. 2017) was detected in the initial UVOT exposures and well detected in all filters. The revised source position was RA(J2000) = 11:09:39.55, Dec(J2000) = −12:35:17.9 (Emery & D'Elia 2017).

The afterglow was tentatively associated with a close-by bright spiral host galaxy at $z = 0.037$ (2MASX J11093966-1235116) even before its optical position was known (Izzo et al. 2017a). Ground-based facilities pointed to the GRB starting a few minutes after the BAT notice, allowing for the detection of the afterglow in the optical and near infrared (e.g., Butler et al. 2017; Mao et al. 2017; Choi & Im 2017; Melandri et al. 2017), and the confirmation of the association with the host galaxy through the detection of both absorption and emission lines at the common redshift of $z = 0.0368$ (Izzo et al. 2017b). The host galaxy mass is $\log_{10} M/M_{\odot} = 10.1 \pm 0.1$, which is at least a factor of ten heavier than any other low-redshift GRB with a confirmed supernova (SN) counterpart (Perley & Taggart 2017), and it has a star-formation rate (SFR) of $3 \pm 1\,M_{\odot}\,\mathrm{yr}^{-1}$. The detection of spectral features from an emerging SN (SN 2017iuk) was indeed reported two days after the burst (de Ugarte Postigo et al. 2017a), with bumps similar to that seen in the very first stages of SN 1998bw (Patat et al. 2001).

Finally, a bright afterglow is also detected in several radio bands (de Ugarte Postigo et al. 2017b; Smith & Tanvir 2017; Perley et al. 2017; Trushkin et al. 2017). As reported by de Ugarte Postigo et al. (2017b) this is the second brightest GRB ever detected at these wavelengths.

3. Data reduction and analysis

3.1. γ-ray data reduction and analysis

3.1.1. BAT data reduction and analysis

The BAT data analysis uses the event-by-event data collected from $T_0 - 239$ s to $T_0 + 963$ s, the standard BAT software (HEASOFT 6.22.1[1]) and the latest calibration database (CALDB[2]). The BAT mask-weighted light curve (Fig. 1) shows some weak overlapping pulses that start at $\sim T_0 - 40$ s and end at $\sim T_0 + 200$ s. T_{90} (15–350 keV) is 190.5 ± 33.9 s (estimated error including systematics). In the following, T_{90} (T_{100}) indicates the time interval where integrated counts from the GRB raise from 5% to 95% (0% to 100%).

The BAT spectral analysis was performed by XSPEC[3]. For the spectrum time period that covers the spacecraft slew time (up

[1] http://heasarc.nasa.gov/lheasoft/
[2] http://heasarc.gsfc.nasa.gov/docs/heasarc/caldb/swift/
[3] http://heasarc.gsfc.nasa.gov/xanadu/xspec/

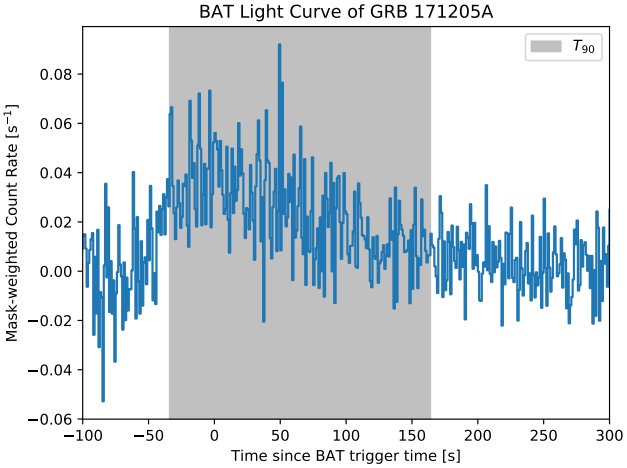

Fig. 1. *Swift*/BAT mask-weighted light curve in 15–350 keV and 1 s time bins. The gray region encloses the T_{90} interval.

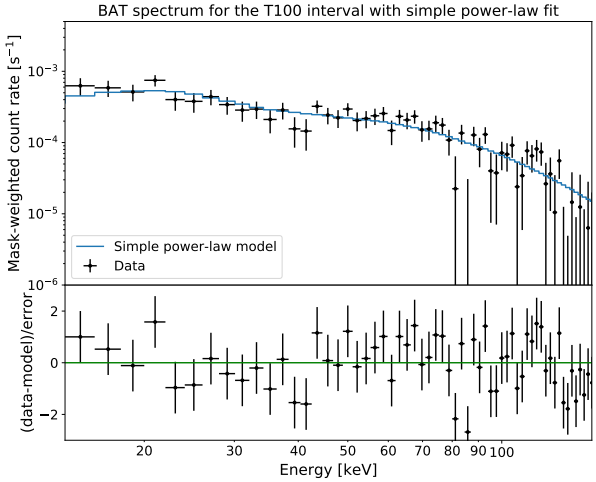

Fig. 2. *Swift*/BAT time averaged spectrum in the T_{100} duration with a simple power-law fit.

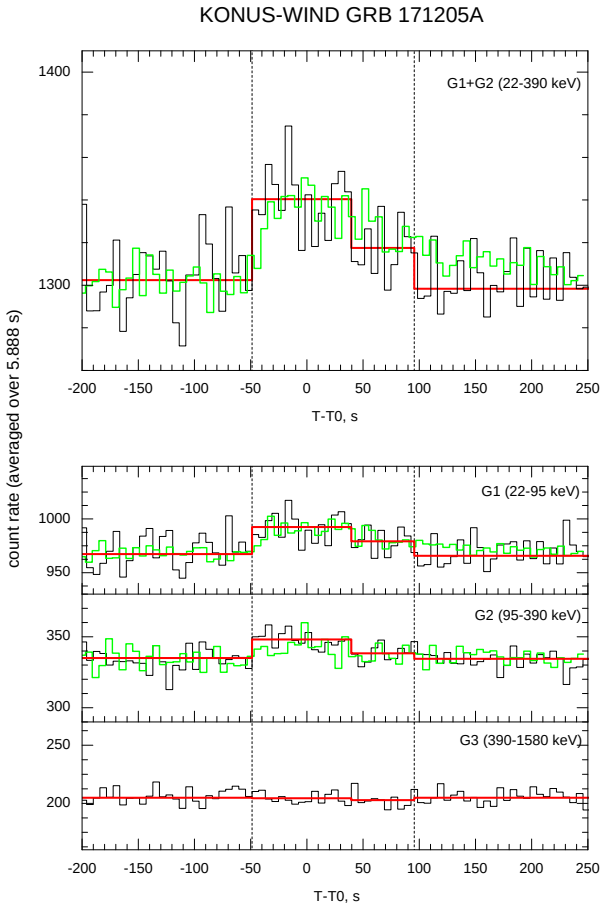

Fig. 3. Konus-*Wind* observation of GRB 171205A in G1+G2, G1, G2, and G3 bands (*top* to *bottom*, black lines). Red lines show the results of the Bayesian block analysis in the G1+G2 band. The *Swift*/BAT light curves in corresponding energy bands are shown for reference (green lines), shifted and scaled to match the KW light curves. The vertical dashed lines denote the data interval chosen for the joint KW+BAT spectral analysis.

to 143 s after the trigger), an average response file is generated by summing up several short-interval (five-second) response files (see detailed description in Lien et al. 2016). The time averaged spectrum from $T_0 - 42.2$ s to $T_0 + 197.8$ s (the T_{100} duration) can be fitted by a simple power-law model with reduced $\chi^2 = 1.08$ for 57° of freedom (d.o.f.). The power law index of the time-averaged spectrum is 1.37 ± 0.14. The cutoff power-law model gives a reduced $\chi^2 = 1.09$ for 56° of freedom (d.o.f.), and hence does not show significant improvement over the simple power-law model. Figure 2 shows the spectrum in the T_{100} duration and the simple power-law fit.

3.1.2. Konus-*Wind* data reduction and analysis

The Konus-*Wind* instrument (KW; Aptekar et al. 1995) is a γ-ray spectrometer consisting of two identical NaI(Tl) detectors, S1 and S2, which observe the southern and northern ecliptic hemispheres, respectively. Each detector has an effective area of 80–160 cm^2, depending on the photon energy and incident angle. Since KW did not trigger on the burst, the data are available only from the instruments "waiting mode". In this mode, count rates with a coarse time resolution of 2.944 s are recorded in three energy bands: G1(22–95 keV), G2(95–390 keV), and G3(390–1580 keV).

A Bayesian block analysis of the KW waiting mode data reveals a weak count rate increase in S1 in the interval from $T_0 - 50$ s to $T_0 + 95$ s. The burst detection significance in the combined G1+G2 light curve is $\sim 10\sigma$ (95 s scale), while no statistically significant emission has been detected in the G3 band (Fig. 3). The time-averaged three-channel spectrum of the most intense part of the burst, measured from $T_0 - 47.797$ s to $T_0 + 41.575$ s, is well fit by a simple power-law (PL) model with the PL index 2.00 ± 0.18, $\chi^2 = 0.88$ for 1 d.o.f.

3.1.3. Konus-*Wind* and *Swift*/BAT joint spectral analysis

To derive the broad-band spectral parameters of this burst, we performed joint spectral analysis of the *Swift*/BAT data and the Konus-*Wind* three-channel spectral data. The energy ranges which we used in the joint spectral analysis are 22–1580 keV and 15–150 keV for the KW and the BAT, respectively. The spectral data of two instruments were fitted in XSPEC with the spectral model multiplied by the constant factor to take into account the systematic effective area uncertainties in the response matrices of each instrument. The resulting BAT constant factor

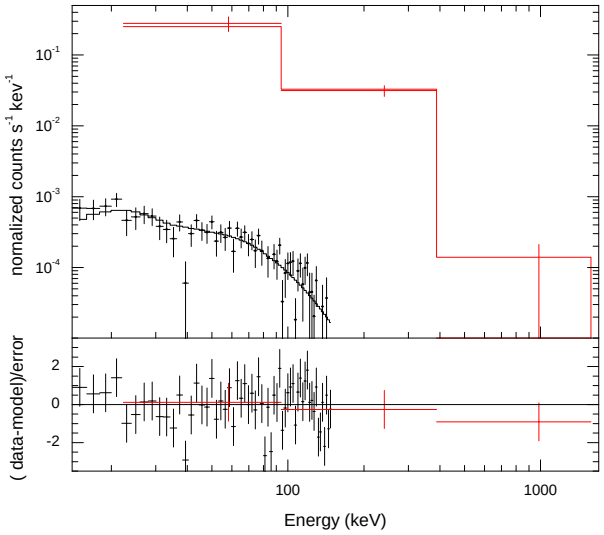

Fig. 4. Konus-*Wind* (red points and line) and *Swift*/BAT (black points and line) joint spectral fit to the time-averaged spectrum with the CPL model.

$C_{\rm BAT}$ (the KW constant factor is fixed to one) is consistent, within uncertainties, with the range (0.8–1.0) derived from the KW–BAT cross-calibration (Sakamoto et al. 2011).

The time interval of the spectral data for each instrument is chosen from $T_0 - 47.797$ to $T_0 + 96.459$ s (to ensure the same spectrum accumulation interval, the KW time has been corrected for the burst propagation from Konus-*Wind* to *Swift*). This interval comprises whole burst as observed by Konus-*Wind* and contains 80% of the total count fluence in the 15–150 keV as observed by BAT.

A fit to the spectrum with a simple power-law function results in a photon index $\alpha = 1.50^{+0.14}_{-0.14}$ with a reduced $\chi^2 = 1.48$ for 59 d.o.f. The reduced χ^2 gives the best agreement adopting as a model a power-law with exponential cutoff (CPL). No systematic residual from the best fit model is seen in the spectral data of each instrument (Fig. 4). The best-fit spectral parameters are: $\alpha = -0.85^{+0.54}_{-0.41}$) and $E_{\rm peak} = 122^{+111}_{-32}$ keV (reduced $\chi^2 = 1.24$ for 58 d.o.f.).

A fit to this spectrum with the Band GRB function yields the same α and $E_{\rm peak}$ and only an upper limit on $\beta < -2.2$ (reduced $\chi^2 = 1.26$ for 57 d.o.f.). The best fit spectral parameters for the Band model fixing β to -2.5 are: $\alpha = -0.88^{+0.57}_{-0.42}$ and $E_{\rm peak} = 125^{+141}_{-37}$ keV (reduced $\chi^2 = 1.27$ for 58 d.o.f.).

To conclude, despite large uncertainties, we are able to constrain both the lower (~90 keV) and the upper (~230 keV) boundary on $E_{\rm peak}$ thanks to the use of the *Swift*/BAT and KW data, respectively, the synergy of the two instruments being the key of the success here. Concerning the spectral model used, assuming a Band model instead of a CPL has little impact on the result, either if we freeze β to -2.5 or if we adopt the hardest spectrum allowed by our data ($\beta < -2.2$, see Table 1).

3.2. XRT data reduction and analysis

Observations of GRB 171205A by *Swift*/XRT were begun about 150 s after the BAT trigger time (T_0 = 2017-12-05 07:20:43 UT); in this first orbit *Swift* collected 9.5 s of data as the satellite was slewing to the target, and 250 s of pointing data in Windowed Timing (WT) mode (D'Elia et al. 2017). *Swift* then regularly monitored the afterglow until 2018 February 21 in PC mode for a total exposure time of ~305 ks. Table A.2 shows the log of all the *Swift*/XRT observations.

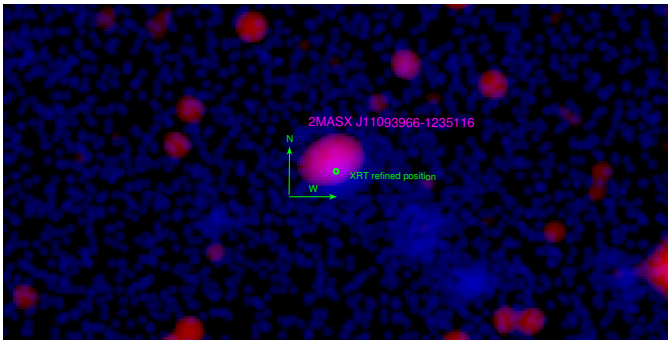

Fig. 5. *Swift*/XRT (0.3–10 keV) data in blue (logarithmic scale) superposed on the optical image from the Sloan Digital Sky Survey in red color. Data are smoothed with a Gaussian kernel of 3 arcsec width and 1.5 arcsec sigma. North and west directions shown by the two arrows of 30 arcsec lenght. The refined XRT position has a radius of 1.5 arcsec and it clearly indicates an offset ~8 arcsec from the center of the host galaxy 2MASX J11093966-1235116.

Table 1. Results of the spectral fit of KW and BAT data from time interval $T_0 - 47.797$ to $T_0 + 96.459$ s.

Instrument	Model	α (PL index)	β (keV)	$E_{\rm peak}$	χ^2 (d.o.f.)
BAT	PL	$1.36^{+0.15}_{-0.15}$	–	–	70.9 (57)
BAT	CPL	$-1.08^{+0.65}_{-0.37}$	–	>94	70.1 (56)
KW	PL	$2.08^{+0.31}_{-0.29}$	–	–	3.9 (1)
KW	CPL	−0.96	–	128	0 (0)
BAT+KW	PL	$1.50^{+0.14}_{-0.14}$	–	–	87.6 (59)
BAT+KW	CPL	$-0.85^{+0.54}_{-0.41}$	–	122^{+111}_{-32}	71.8 (58)
BAT+KW	Band	$-0.85^{+0.54}_{-0.41}$	< -2.2	123^{+111}_{-32}	71.8 (57)
BAT+KW	Band	$-0.88^{+0.57}_{-0.42}$	−2.5 (fixed)	125^{+141}_{-37}	73.3 (58)
BAT+KW	Band	$-0.91^{+0.32}_{-0.41}$	−2.2 (fixed)	128^{+170}_{-42}	74.6 (58)

The data were processed using the XRTDAS software (v. 3.4.0; Capalbi et al. 2005) developed at the ASI Space Science Data Center and included in the HEAsoft package (v. 6.22.1) distributed by HEASARC. For each observation of the sample, calibrated and cleaned WT and PC mode event files were produced with the *xrtpipeline* task. The default screening criteria were applied to the data.

For PC (WT) data, we extracted high-level scientific products using a circular (strip) region of 20 pixel radius (one pixel = 2.36″) centered on source in the 0.3–10 keV energy range. We choose as the background a region of similar area next to the afterglow position where no other contaminating source is present. In Fig. 5 we show the field of GRB 171205A, obtained superposing the XRT refined position to the optical image from the Sloan Digital Sky Survey.

The X-ray light curve of the afterglow can be well described by a steep (index 2.2) power-law from $T_0 + 300$ s to $T_0 + 7.2$ ks, followed by a plateau phase (index ~ 0) from $T_0 + 7.2$ ks to $T_0 + 92$ ks, followed by a power-law decay of index 1.08, in other words, a typical steep-flat-normal behavior (Kennea et al. 2017). The data before $T_0 + 300$ s are described by a shallower power-law (index 1.8) with respect to the steep decay. The XRT light curve is reported in Fig. 6.

During the first XRT observation performed in WT mode, from 150 s to 400 s after the BAT trigger, the residuals in the softest XRT band suggested the presence of an additional thermal

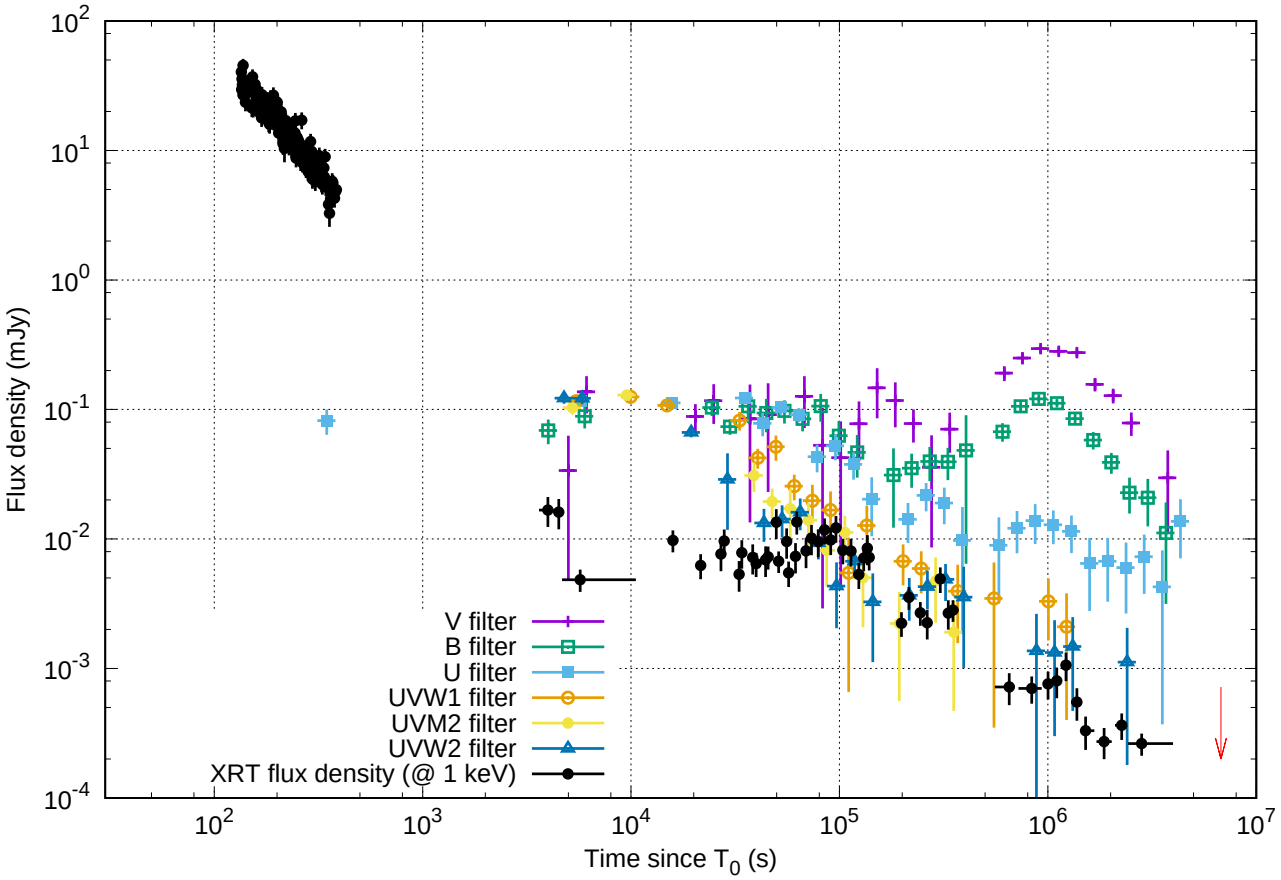

Fig. 6. *Swift*/XRT and *Swift*/UVOT light curve of the GRB 171205A afterglow. UVOT data are corrected for the host galaxy and extinction contribution. Information on the UVOT filter passbands can be found at: http://www.swift.ac.uk/analysis/uvot/filters.php

component (Campana et al. 2017). We divided the XRT spectral data into two datasets each containing an equal number of photons (splitting the observation at ~225 s after trigger). We then fit the two datasets to investigate spectral changes, but we find compatible results between the two datasets. To better investigate the presence of a soft component we included in the fit also the 45 s of BAT data contemporaneous with the XRT observations. We fit the BAT+XRT data with a power law plus a blackbody component plus a Galactic absorption component (fixed to 5.9×10^{20} cm^{-2}, Willingale et al. 2013, modeled with `tbabs`). The soft blackbody component is significant based on an F-test (F statistic value = 19.2608 and probability of null hypotesis = 1.7×10^{-8}. We also included an intrinsic absorption component at the redshift $z = 0.0368$ of the host galaxy (Izzo et al. 2017b). The inclusion of this additional absorption component is significant at 0.4% (F-test). The overall fit is good, with reduced $\chi^2 = 0.99$ for 246 d.o.f. The blackbody temperature is 89^{+13}_{-9} eV and its radius at 163 Mpc is $1.5^{+1.2}_{-0.7} \times 10^{12}$ cm. The intrinsic absorption is $9^{+6}_{-5} \times 10^{20}$ cm^{-2}. The power law photon index is $\Gamma = 1.64 \pm 0.07$. The mean 0.3–10 keV unabsorbed flux during the WT observation is 1.5×10^{-9} erg cm^{-2} s^{-1} (corresponding to a luminosity of 4.8×10^{45} erg s^{-1}), with the blackbody component comprising ~20%. We show in Fig. 7 the XRT unfolded spectrum of the best fit model, including the blackbody component, together with the residuals.

We time-selected the PC-mode data and extracted energy spectra in correspondence with the time intervals having the same decay index in the light curve. We adopted a power law spectrum, imposing the same absorption column on the

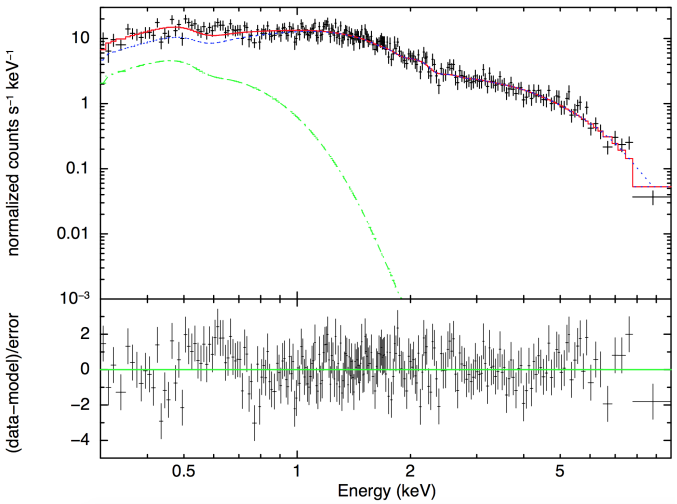

Fig. 7. *Top panel*: *Swift*/XRT (0.3–10 keV) unfolded spectrum and best-fit model (blackbody component in green and power-law in blue). *Bottom panel*: residuals of the fit to the data.

BAT+WT-mode and PC-mode spectra and we found no significant change in slope of the power-law ($\Gamma = 1.83 \pm 0.06$). We therefore averaged all the data in PC mode and made a common fit with the WT data. The intrinsic host-galaxy absorption is further constrained to be $7.4^{+4.1}_{-3.6} \times 10^{20}$ cm^{-2} at the host redshift of $z = 0.0368$ (see Fig. 8). The parameters of the (WT) blackbody changed to 91^{+11}_{-9} eV for the temperature, and $1.3^{+0.8}_{-0.5} \times 10^{12}$ cm

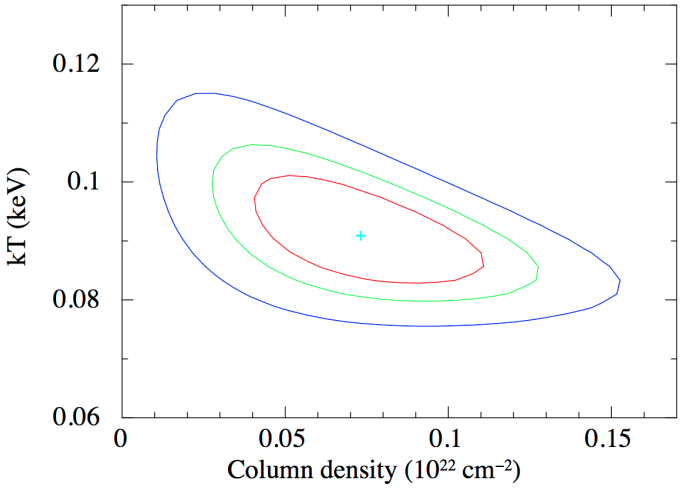

Fig. 8. Contour plot showing intrinsic column density vs. temperature for the combined WT and late time PC spectrum. Red, green and blue curves enclose 1σ, 2σ and 3σ confidence contours, respectively.

for the radius at 163 Mpc ($\Gamma = 1.63 \pm 0.06$), that is, they are consistent within the errors. The blackbody component is still comprising ~17% of the 0.3–10 keV flux. The overall fit is good with reduced $\chi^2 = 0.97$ for 284 d.o.f. To conclude, we note the intrinsic X-ray column density we obtain is at the low end of the GRB distribution, even among low redshift *Swift*/XRT GRBs where the mean is $N_{\rm H,int} \sim 2.4 \times 10^{21}$ cm^{-2} at $z < 0.2$ (Arcodia et al. 2016).

3.3. UVOT data reduction

The *Swift*/UVOT began observing the field of GRB 171205A 154 s after the trigger (D'Elia et al. 2017). The afterglow was detected in all UVOT filters.

The source counts were extracted using a region of 3″ radius. We used this aperture size because whilst the standard aperture for extracting count rates is a 5″ radius aperture, it is more accurate to use a smaller source aperture if the count rate is low (Poole et al. 2008). Furthermore, a smaller aperture limited the contamination of the host galaxy. The count rates were corrected to a 5″ aperture using the curve of growth from the UVOT calibration files so that they are consistent with the UVOT calibration. Background counts were extracted using a circular region of radius 30″ in a source-free region where the is no substantial contribution from the host galaxy. The count rates were measured using the *Swift* ftool *uvotsource* and were converted to magnitudes using the UVOT photometric zero points (Breeveld et al. 2011). The UVOT data are provided in Table A.2. The analysis pipeline used software HEADAS 6.21 and UVOT calibration 20170130.

Since we observed GRB 171205A superposed on its host galaxy, the count rates we measured are contaminated with light from the host. To measure the contribution of the host galaxy, we measured the count rates for each observation between 6729–6788 ks using the same 3″ source aperture we used for GRB 171205A and performed a moving mean calculation to get an average count rate for the host galaxy. The host galaxy count rates were aperture-corrected to 5″ for the same reasons as the source count rates were. Host galaxy correction was performed on all count rates for each filter.

For each light curve the magnitudes were binned with $\Delta t/t = 0.2$, when the signal-to-noise ratio, $(S/N) < 2$. Additionally, the light curves were adjusted to correct for Galactic extinction, $E(B-V) = 0.0434$ (Schlafly & Finkbeiner 2011). The resulting background subtracted, galactic extinction corrected light curves are displayed in Fig. 6. No correction for the host galaxy absorption was performed.

4. Discussion

4.1. γ-ray energetics and spectral shape

Using the joint BAT and Konus-*Wind* spectral fit, the burst energy fluence in the 15–1500 keV band calculated by the best-fit (CPL) model for the 144.26 s interval is $S = 5.98^{+1.8}_{-1.41} \times 10^{-6}$ erg cm^{-2}. Assuming $z = 0.0368$ (Izzo et al. 2017b), we estimated the isotropic energy release (1 keV–10 MeV in the GRB rest frame) of GRB 171205A to be $E_{\rm iso} = 2.18^{+0.63}_{-0.50} \times 10^{49}$ erg.

In this approach, the $E_{\rm iso}$ errors are propagated directly from the flux errors, that is, not taking into account the k-correction uncertainty. We checked that, calculating the model fluence in the bolometric rest-frame band to take this effect into account, increases just slightly the $E_{\rm iso}$ error (less than 10%). Concerning the spectral model uncertainties, if we use a Band function instead of a CPL, we obtain $E_{\rm iso} = 3.6^{+0.9}_{-0.9} \times 10^{49}$, a slightly higher value.

The $E_{\rm iso}$ derived for this burst is similar to those of other low-luminosity GRBs. For example, the $E_{\rm iso}$ (in the observed 15–150 keV band) for GRB 060218 is 2.57×10^{49} erg (assuming $T_{90} = 2100$ s, see Campana et al. 2006) and GRB 100316D has $E_{\rm iso} \geq 3.70 \times 10^{49}$ erg (assuming $T_{90} \geq 1300$ s, see Starling et al. 2011). However, besides the low $E_{\rm iso}$, other properties of GRB 171205A seem to be different from GRB 060218 and GRB 100316D. The BAT spectrum of GRB 171205A is harder than those of GRB 060218 and GRB 100316D, which have power-law indices of 2.18 and 2.36, respectively (Lien et al. 2016). In addition, both GRB 060218 and GRB 100316D show long-lasting burst emission of more than ~1000 s, while GRB 171205A has no obvious emission after $\sim T_0 + 200$ s, though we note that GRB 171205A went out of the BAT field of view at $T_0 + 479$ s. As shown in Fig. 9, GRB 171205A lies outside the Amati relation from the BAT long GRB (Krimm et al. 2009) and the Konus-*Wind* (Tsvetkova et al. 2017) samples, even adopting the more conservative values for $E_{\rm peak}$ (see Sect. 3.1.3) and $E_{\rm iso}$.

Other low-luminosity GRBs such as 171205A are not consistent with the Amati relation. As discussed by Amati et al. 2007, this lack of consistency strongly indicates that these LL-GRBs are not just normal, "cosmological" events seen off-axis. GRBs are supposed to be jetted sources seen on-axis (Sari et al. 1999) or very close to it. Theoretically, if a GRB event were seen off-axis, the prompt emission detected would be weaker, since the radiation is strongly beamed toward the direction of motion by relativistic effects. It is found that $E_{\rm p} \propto \delta$ and $E_{\rm iso} \propto \delta^{1-\alpha}$ (Amati et al. 2007; Yamazaki et al. 2003), where α is the low-energy photon index and δ is the relativistic Dopper factor which, in turn, depends on the half-opening angle $\theta_{\rm jet}$ of the GRB jets and the angle between the GRB jet axis and the observer $\theta_{\rm obs}$: $\delta = (\Gamma(1 - \nu/c\cos(\theta_{\rm obs} - \theta_{\rm jet})))^{-1}$. This parameter δ decreases as $\theta_{obs} - \theta_{\rm jet}$ increases.

Since $E_{\rm p}$ and $E_{\rm iso}$ depend on δ in different ways, GRBs seen off-axis cannot follow the Amati relation as GRBs seen on-axis. We find that, in principle, this might be the case for 171205A. Let us assume $\alpha = -1.2$, which is still consistent with the analysis of the prompt emission at 90% confidence level. Let us also assume that this GRB is seen off-axis and that δ decreases by a factor of ~500 from when this event is observed on-axis. Thus,

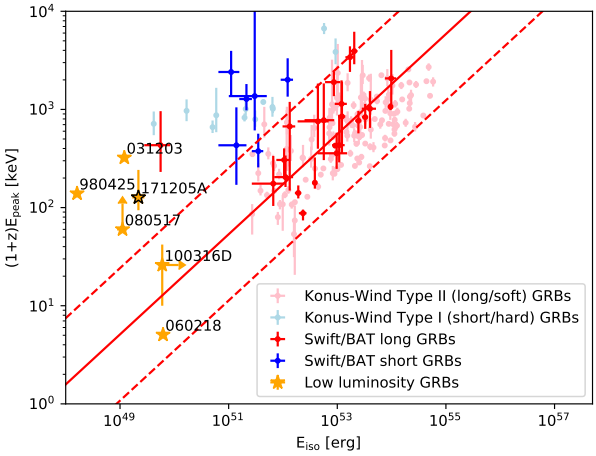

Fig. 9. $E_{\rm peak}$ in rest-frame versus $E_{\rm iso}$. The *Swift*/BAT GRB sample (dark blue and red) is adapted from Krimm et al. (2009). The Konus-*Wind* GRB sample (light blue and red) is adapted from Tsvetkova et al. (2017). The yellow stars show GRB 171205A and several sources defined as low-luminosity GRBs in previous studies (Campana et al. 2006; Ghisellini et al. 2006; Starling et al. 2011; Stanway et al. 2015). The red lines are the best fit (solid line) and the 2.5σ variation (dashed line) reported in Krimm et al. (2009).

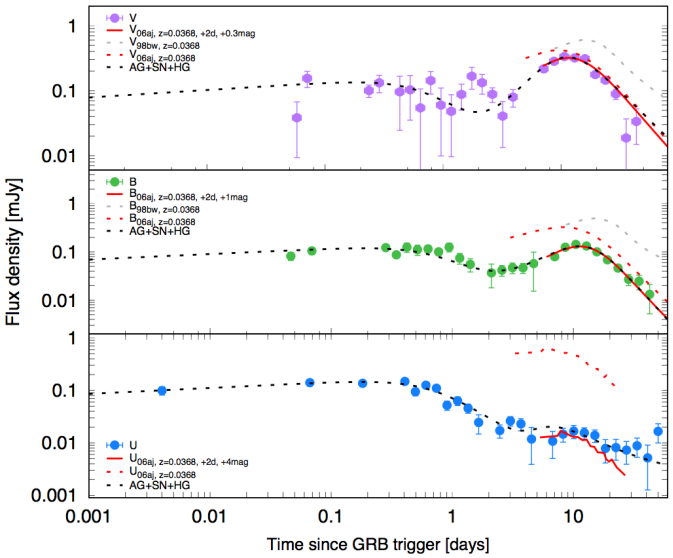

Fig. 10. Overall fit of the *ubv* light curves (dashed black line). The best match for the SN contribution is obtained with the SN 2006aj template (dashed red lines) shifted by +2 days but lower in magnitude (solid red lines).

the estimate of $E_{\rm p}$ would decrease by ~500, while the estimate of $E_{\rm iso}$ would decrease by $\sim 500^{1+1.2} = 8.7\times10^5$. The on-axis values of these parameters would thus be $E_{\rm p,on\,axis} \sim 6\times10^4$ keV and $E_{\rm iso,on\,axis} \sim 2\times10^{56}$ erg. In principle, these estimates are now within ~2.5σ variation from the best fit of the Amati relation. However, these values are also highly problematic because they are large compared to those of known GRBs. A GRB with such parameters would be truly exceptional and unlikely to be found within the relatively small volume enclosed by the redshift of GRB 171205A. A higher value of α would only exacerbate the problem, while lower values of δ would not allow the parameters of this GRB to be consistent with the Amati relation. Thus, GRB 171205A seems to be an event that cannot be explained as a typical cosmological event seen off-axis; instead, its emission mechanism appears to be different from those of farther away, very energetic GRBs.

We conclude the section with a word of caution on the outliers of the Amati relation. The relation below 10^{50} erg is not well studied yet, and in some cases the locations of the outliers could be due to observational biases (Martone et al. 2017). In addition, the upper boundary of the Amati relation, as distinct from the lower one, is strongly affected by instrumental selection effects (Heussaff et al. 2013; Tsvetkova et al. 2017) and could not be unequivocally treated as an intrinsic GRB property. Thus, the problem of the upper-side outliers in the Amati relation, especially at low $E_{\rm iso}$, is rather complicated.

4.2. The UV-optical light curve

At early times, the UV-optical light curves (Fig. 6) are flat ($\alpha_{1,U} = -0.11\pm0.08$), consistent with the plateau phase observed in the X-rays, followed by a steeper decay phase ($\alpha_{2,U} = 1.79 \pm 0.39$). This behaviour has been previously observed for several *Swift* GRBs (i.e., Oates et al. 2009; Melandri et al. 2014). At late times ($\Delta t > 3$ d) the signature of an emerging supernova component is clearly visible in the *UBV* optical filters, and this was also reported by independent spectroscopic observations (de Ugarte Postigo et al. 2017a).

In Fig. 10 we fit the early *u*-band light curve (which is the best sampled filter since the start of UVOT observations) with a broken power-law in order to estimate the afterglow contribution. The best fit is then rigidly shifted to the *b* and *v*-band data. The agreement with the data is good and therefore we can consider the UVOT afterglow to be achromatic. Then we compare the observed *u*, *b*, and *v* light curves for SN 2017iuk with the corresponding curves for SN 1998bw and SN 2006aj. The best match of the SN bump is with the template light curves of SN 2006aj, but lower in magnitude and with the peak time shifted by ~2 d. A simple estimate of the peak time for the *b* and *v* filters provides the following values: $t^B_{\rm peak} = 12.7\pm1.2$ and $t^V_{\rm peak} = 13.6\pm1.5$ days. These values are consistent with typical peak times and magnitudes of other well-studied SNe connected with low-luminous GRBs (i.e., Cano et al. 2017a). Finally, we summed the afterglow, supernova, and host galaxy contribution obtaining the overall fit of the light curves in the *UBV* filters (Fig. 10).

The description of the properties of SN 2017iuk is beyond the purpose of this paper and it would require a more detailed modeling and subtraction of the afterglow contribution in each UVOT filter. However, we must note that despite the fact that the behaviour of the UV-optical light curve at $t < 5$ d seems to be achromatic, it displays a possible premaximum bump in the *v*-band that is not visible in other filters. As discussed by Cano et al. (2017b) such early bumps have been observed for other GRBs–SNe and they typically seem to be achromatic; for SN 2017iuk (as for SN 2016jca, discussed by Cano et al. 2017b) the bump is detected only in one filter and its physical origin could not be easily explained.

4.3. X-ray spectral behaviour

Although the X-ray spectrum is well described by an absorbed power law, the inclusion of a thermal component to fit the data significantly improves the reduced χ^2 (see Sect. 3.2). The presence of such a component is not new in GRB spectra, especially in the early time data of GRBs associated with SNe, with notable examples being GRB 060218 (e.g., Campana et al. 2006),

GRB 090618 (e.g., Page et al. 2011) and GRB 100316D (e.g., Starling et al. 2011).

The origin of this thermal feature in GRBs is still under debate, with one of the first proposed explanations being the shock breakout of the emerging supernova (Colgate 1974; Waxman et al. 2007; Nakar & Sari 2010, 2012). Alternative explanations include late jet photospheric emission (e.g., Friis & Watson 2013), or that the emission comes from a relativistically expanding hot plasma cocoon surrounding the GRB jet (e.g., Suzuki & Shigeyama 2013; De Colle et al. 2018). In fact, Pe'er et al. (2006) demonstrate that a few hundreds of seconds after the prompt emission, the bulk of the cocoon radiation may fall in the X-ray band.

The first attempt to study the X-ray thermal emission in GRB–SNe from a statistical point of view was performed by Starling et al. (2012). These authors select 11 *Swift* GRBs with associated SNe and systematically searched for a thermal (blackbody-like) emission in the X-ray spectra. They found that four objects do (and three do not) show this component, and identified a further four possible cases of thermal emission. The conditions on redshift and absorbing column density required for detection of a thermal X-ray component similar to those seen previously in GRB afterglows are assessed in Sparre & Starling (2012) and are all met in the case of GRB 171205A. We therefore compared the physical parameters of the Starling et al. sample with those evaluated for our GRB. The ratio between the blackbody and the total 0.3–10 keV X-ray flux as well as the radius of the blackbody emitting region for GRB 171205A fall within the corresponding parameter distributions reported in Starling et al. (2012). On the other hand, our GRB has a blackbody temperature that is lower than those of all GRBs reported in Starling et al. (2012) over the first few hundred seconds since burst (thanks also to the closeness of the GRB), but is consistent with their later (~760 s) detections of the blackbody in GRB 101219B .

5. Conclusions

The burst GRB 171205A revealed itself as a close-by burst (z = 0.0368), thus belonging to a class of GRBs comprising few but high flux events. Together with the discovery of the associated supernova (SN 2017iuk), this made GRB 171205A one of the most followed-up bursts of recent years.

In this paper we presented the *Swift* and Konus-*Wind* data of this burst. The dataset extends up to $\sim 10^7$ s in the time domain and from the *Swift*/UVOT v band ($\sim 2.25 \times 10^{-3}$ keV) to the highest Konus-*Wind* band ($\sim 1.6 \times 10^3$ keV).

Our main findings are summarized below.

– We derive the rest frame peak energy $E_{\rm p} = 125^{+141}_{-37}$ keV and isotropic energy $E_{\rm iso} = 2.18^{+0.63}_{-0.50} \times 10^{49}$ erg by fitting the *Swift*/BAT and Konus-*Wind* spectral data. As other low luminosity GRBs, GRB 171205A lies outside the Amati relation. This behaviour strongly indicates that this GRB is not a "normal" event seen off-axis, but its emission mechanism should be different from cosmological bursts.

– We studied the optical-UV light curve collected by *Swift*/UVOT. The v, b, and u data clearly show a supernova feature emerging from the fading contribution of the afterglow radiation. The peak of the SN emission is located at ~13 days after the GRB detection. Comparing SN 2017iuk light curves with templates in the literature, we found that the best match is with SN 2006aj, but lower in magnitude and with the peak time shifted by approximately two days. We finally note a premaximum bump in the v-band. Such features have been observed in other GRB-associated SNe, but not in just a sinlge band as in GRB 171205A (i.e., the premaximum bump was achromatic). The chromaticity of the premaximum bump in the GRB 171205A/SN 2017iuk is thus not easily explained.

– We produced the X-ray spectrum of GRB 171205A using the *Swift*/XRT data. The intrinsic column density lies at the low end of the GRB distribution, even considering just low redshift *Swift*/XRT GRBs. We detected a thermal component in the X-ray spectrum. The ratio between the blackbody and the total 0.3–10 keV X-ray flux as well as the radius of the blackbody emitting region for GRB 171205A fall within the the corresponding parameter distributions reported in previous works. On the other hand, our GRB has a blackbody temperature that is lower than that of all GRBs with a reported thermal component at early times. The origin of this component is still a matter of debate.

Acknowledgements. The *Swift* team would like to devote this paper to the memory of Neil Gehrels. RLCS acknowledges funding from STFC. KLP and JPO acknowledge support from the UK Space Agency. DDF, DSS, and AET acknowledge support from RSF grant 17-12-01378. DNB and AT acknowledge support from NASA contract NAS5-00136. SRO gratefully acknowledges the support of the Leverhulme Trust Early Career Fellowship.

References

Amati, L., Della Valle, M., Frontera, F., et al. 2007, A&A, 463, 913
Aptekar, R. L., Frederiks, D. D., Golenetskii, S. V., et al. 1995, Space Sci. Rev., 71, 265
Arcodia, R., Campana, S., & Salvaterra, R. 2016, A&A, 590, A82
Barniol Duran, R., Nakar, E., Piran, T., & Sari, R. 2015, MNRAS, 448, 417
Barthelmy, S. D., Barbier, L. M., Cummings, J. R., et al. 2005, Space Sci. Rev., 120, 143
Barthelmy, S. D., Cummings, J. R., D'Elia, V., et al. 2017, GCN Circ., 22184
Berger, E., Fox, D. B., Kulkarni, S. R., Frail, D. A., & Djorgovski, S. G. 2007, ApJ, 660, 504
Breeveld, A. A., Landsman, W., Holland, S. T., et al. 2011, AIPC, 1358, 373
Bufano, F., Pian, E., Sollerman, J., et al. 2012, ApJ, 753, 67
Burrows, D. N., Hill, J. E., Nousek, J. A., et al. 2005, Space Sci. Rev., 120, 165
Butler, N., Watson, A. M., Kutyrev, A., et al. 2017, GCN Circ., 22182
Campana, S., Mangano, V., Blustin, A. J., et al. 2006, Nature, 442, 1008
Campana, S., Beardmore, A., D'A, A., et al. 2017, GCN Circ., 22191
Cano, Z., Wang, S.-Q., Dai, Z.-G., Wu, X.-F., et al. 2017a, Adv. Astron., 2017, 8929054
Cano, Z., Izzo, L., de Ugarte Postigo, A., et al. 2017b, A&A, 605, A107
Capalbi, M., Perri, M., Saija, B., Tamburelli, F., & Angelini, L. 2005, http://heasarc.nasa.gov/docs/swift/analysis/xrt_swguide_v1_2.pdf
Choi, C., & Im, M. 2017, GCN Circ., 22188
Colgate, S. A. 1974, ApJ, 187, 333
Cucchiara, A., Levan, A. J., Fox, D. B., et al. 2011, ApJ, 736, 7
Cusumano, G., Mangano, V., Chincarini, G., et al. 2006, A&A, 462, 73
Daigne, F., & Mochkovitch, R. 2007, A&A, 465, 1
De Colle, F., Lu, W., Kumar, P., Ramirez-Ruiz, E., & Smoot, G. 2018, MNRAS, 478, 4553
D'Elia, V., D'A, A., Lien, A. Y., & Sbarufatti, B. 2017, GCN Circ., 22177
Della Valle, M., Chincarini, G., Panagia, N., et al. 2006, Nature, 444, 1050
Dereli, H., Boer, M., Gendre, B., et al. 2017, ApJ, 850, 117
de Ugarte Postigo, A., Izzo, L., & Kann, D. A. 2017a, GCN Circ., 22204
de Ugarte Postigo, A., Schulze, S., & Bremer, M. 2017b, GCN Circ., 22187
Emery, S. W. K., & D'Elia, V. 2017, GCN Circ., 22181
Fan, Y. Z., Zhang, B. B., Xu, D., Liang, E. W., & Zhang, B. 2011, ApJ, 726, 32
Frederiks, D., Golenetskii, S., & Aptekar, R. 2017, GCN Circ., 22227
Friis, M., & Watson, D. 2013, ApJ, 771, 15
Fryer, C. L., Rueda, J. A., & Ruffini, R. 2014, ApJ, 793, L36
Fynbo, J. P. U., Starling, R. L. C., Ledoux, C., et al. 2006a, A&A, 451, L47
Fynbo, J. P. U., Watson, D., Thöne, C. C., et al. 2006b, Nature, 444, 1047
Galama, T. J., Vreeswijk, P. M., van Paradijs, J., et al. 1998, Nature, 395, 670
Gehrels, N., Chincarini, G., Giommi, P., et al. 2004, ApJ, 621, 558
Ghisellini, G., Ghirlanda, G., Mereghetti, S., et al. 2006, MNRAS, 372, 1699
Heussaff, V., Atteia, J.-L., & Zolnierowski, Y. 2013, A&A, 557, A100
Hjorth, J., & Bloom, J. S. 2012, in Gamma-Ray Bursts, eds. C. Kouveliotou, R. A. M. J. Wijers, & S. E. Woosley (Cambridge: Cambridge Univ. Press)

Hjorth, J., Sollerman, J., Møller, P., et al. 2003, Nature, 423, 847
Izzo, L., Kann, D. A., Fynbo, J. P. U., Levan, A. J., & Tanvir, N. R. 2017a, GCN Circ., 22178
Izzo, L., Selsing, J., & Japelj, J. 2017b, GCN Circ., 22180
Kalberla, P. M. W., Burton, W. B., Hartmann, D., et al. 2005, A&A, 440, 775
Kennea, J. A., Sbarufatti, B., & Burrows, D. N. 2017, GCN Circ., 22183
Krimm, H. A., Yamaoka, K., Sugita, S., et al. 2009, ApJ, 704, 1405
Krühler, T., Malesani, D., Fynbo, J. P. U., et al. 2015, A&A, 581, A125
Kulkarni, S. R., Frail, D. A., Wieringa, M. H., et al. 1998, Nature, 395, 663
Lien, A. Y., Sakamoto, T., Barthelmy, S. D., et al. 2016, ApJ, 829, 7
MacFadyen, A. I., & Woosley, S. E. 1999, ApJ, 524, 262
Malesani, D., Tagliaferri, G., Chincarini, G., et al. 2004, ApJ, 609, L5
Mao, J., Ding, X., & Bai, J. M. 2017, GCN Circ., 22186
Martone, R., Izzo, L., Della Valle, M., et al. 2017, A&A, 608, A52
Maselli, A., Melandri, A., Nava, L., et al. 2013, Science, 343, 48
Mazzali, P. A., Deng, J., Pian, E., et al. 2006a, ApJ, 645, 1323
Mazzali, P. A., Deng, J., Nomoto, K., et al. 2006b, Nature, 442, 1018
Melandri, A., Covino, S., Rogantini, D., et al. 2014, A&A, 565, A72
Melandri, A., Melandri, A., & D'Avanzo, P. 2017, GCN Circ., 22189
Mészáros, P. 2006, Rep. Prog. Phys., 69, 2259
Nakar, E., & Sari, R. 2010, ApJ, 725, 904
Nakar, E., & Sari, R. 2012, ApJ, 747, 88
Oates, S. R., Page, M. J., Schady, P., et al. 2009, MNRAS, 395, 490
Osborne, J. P., Beardmore, A. P., Evans, P. A., & Goad, M. R. 2017, GCN Circ., 22179
Paczynski, B. 1998, ApJ, 494, L45
Page, K. L., Starling, R. L. C., Fitzpatrick, G., et al. 2011, MNRAS, 416, 2078
Patat, F., Cappellaro, E., Danziger, J., et al. 2001, ApJ, 555, 900
Pe'er, A., Mészáros, P., & Rees, M. J. 2006, ApJ, 652, 482
Perley, D.A., & Taggart, K. 2017, GCN Circ., 22194
Perley, D.A., Schulze, S., & de Ugarte Postigo, A. 2017, GCN Circ., 22252
Pian, E., Mazzali, P. A., Masetti, N., et al. 2006, Nature, 442, 1011
Planck Collaboration XVI. 2014, A&A, 571, A16
Poole, T. S., Breeveld, A. A., Page, M. J., et al. 2008, MNRAS, 383, 627
Prochaska, J. X., Chen, H. W., Dessauges-Zavadsky, E., & Bloom, J. S. 2007, ApJ, 666, 267
Racusin, J. L., Karpov, S. V., Sokolowski, M., et al. 2008, Nature, 455, 183
Roming, P. W. A., Kennedy, T. A., Masono, K. O., et al. 2005, Space Sci. Rev., 120, 95
Sakamoto, T., Pal'Shin, V., Yamaoka, K., et al. 2011, PASJ, 63, 215
Salvaterra, R., Della Valle, M., Campana, S., et al. 2009, Nature, 461, 1258
Sari, R., Piran, T., & Halpern, J. P. 1999, ApJ, 519, L17
Smith, I. A., & Tanvir, N. R. 2017, GCN Circ., 22242
Soderberg, A. M., Kulkarni, S. R., Berger, E., et al. 2004, Nature, 430, 648
Sparre, M., & Starling, R. L. C. 2012, MNRAS, 427, 2965
Sparre, M., Hartoog, O. E., Krühler, T., et al. 2014, ApJ, 785, 150
Stanek, K. Z., Matheson, T., Garnavich, P. M., et al. 2003, ApJ, 591, L17
Stanway, E. R., Levan, A. J., Tanvir, N., et al. 2015, MNRAS, 446, 3911
Starling, R. L. C., Wiersema, K., Levan, A. J., et al. 2011, MNRAS, 411, 2792
Starling, R. L. C., Page, K. L., Pe'er, A., Beardmore, A. P., & Osborne, J. P. 2012, MNRAS, 427, 2950
Suzuki, A., & Shigeyama, T. 2013, ApJ, 764, L12
Tanvir, N. R., Fox, D. B., Levan, A. J., et al. 2009, Nature, 461, 1254
Trushkin, S. A., Erkenov, A. K., Tsybulev, P. G., & Nizhelskij, N. A. 2017, GCN Circ., 22258
Tsvetkova, A., Frederiks, D., Golenetskii, S., et al. 2017, ApJ, 850, 161
Virgili, F. J., Liang, E. W., & Zhang, B. 2009, MNRAS, 392, 91
Vreeswijk, P. M., Fruchter, A., Kaper, L., et al. 2001, ApJ, 546, 672
Watson, D., Hjorth, J., Levan, A., et al. 2004, ApJ, 605, L101
Waxman, E., Mészáros, P., & Campana, S. 2007, ApJ, 667, 351
Willingale, R., Starling, R. L. C., Beardmore, A. P., Tanvir, N. R., & O'Brien, P. T. 2013, MNRAS, 431, 394
Woosley, S. E. 1993, ApJ, 405, 273
Woosley, S. E., & Bloom, J. S. 2006, ARA&A, 44, 507
Yamazaki, R., Yonetoku, D., & Nakamura, T. 2003, ApJ, 594, L79

Appendix A: Summary of our XRT and UVOT observations

Table A.1. Log of the *Swift*/XRT observations used in this work.

ObsID (MODE)	T_{start}(TT)	T_{stop} (TT)	Exposure (s)	Count rate/Error (10^{-3} counts s^{-1})
794972000 (WT)	2017-12-05 07:23:30	2017-12-05 08:21:12	250	$(24.6 \pm 0.3) \times 10^3$
794972000 (PC)	2017-12-05 08:21:14	2017-12-05 08:25:04	229	29 ± 13
794972001 (PC)	2017-12-05 08:29:14	2017-12-05 15:14:52	7964	19.0 ± 1.7
794972002 (PC)	2017-12-05 16:19:40	2017-12-06 22:40:54	14724	16.7 ± 1.2
794972003 (PC)	2017-12-06 00:31:46	2017-12-06 22:55:52	19968	7.3 ± 1.3
794972004 (PC)	2017-12-07 14:36:22	2017-12-07 21:17:53	7302	7.2 ± 1.2
794972005 (PC)	2017-12-07 11:33:22	2017-12-07 13:23:52	1753	8.1 ± 2.5
794972006 (PC)	2017-12-08 00:10:04	2017-12-08 09:59:52	7921	6.7 ± 1.1
794972007 (PC)	2017-12-08 19:15:11	2017-12-08 21:14:54	2040	1.3 ± 0.3
794972008 (PC)	2017-12-09 00:07:23	2017-12-09 13:10:53	7354	7.8 ± 1.6
794972009 (PC)	2017-12-09 14:47:03	2017-12-09 14:47:03	759	1.9 (3-σ u.l.)
794972010 (PC)	2017-12-11 17:54:11	2017-12-11 21:09:54	702	2.4 (3-σ u.l.)
794972012 (PC)	2017-12-12 12:32:17	2017-12-12 19:24:52	7497	1.6 ± 0.6
794972014 (PC)	2017-12-13 01:45:15	2017-12-13 17:49:54	4747	2.0 ± 0.8
794972015 (PC)	2017-12-13 19:13:05	2017-12-13 19:26:55	812	2.1 (3-σ u.l.)
794972016 (PC)	2017-12-14 01:15:54	2017-12-14 14:24:53	4915	2.0 ± 0.9
794972017 (PC)	2017-12-15 01:12:53	2017-12-15 23:51:52	5996	2.7 ± 0.8
794972018 (PC)	2017-12-16 01:07:53	2017-12-16 23:54:53	9607	2.0 ± 0.5
794972019 (PC)	2017-12-17 01:16:25	2017-12-17 18:47:52	7165	1.4 ± 0.7
794972020 (PC)	2017-12-18 00:48:53	2017-12-18 10:38:53	5436	3.1 ± 0.9
794972021 (PC)	2017-12-19 00:57:56	2017-12-19 16:57:53	8480	3.0 ± 0.7
794972022 (PC)	2017-12-20 05:54:20	2017-12-20 20:03:53	6545	2.2 ± 0.8
794972023 (PC)	2017-12-21 00:42:03	2017-12-21 18:35:54	8213	2.1 ± 0.6
794972024 (PC)	2017-12-21 19:47:23	2017-12-22 11:58:54	8121	1.3 ± 0.5
794972025 (PC)	2017-12-23 02:33:21	2017-12-23 13:35:51	5614	1.0 ± 0.5
794972026 (PC)	2017-12-24 02:22:53	2017-12-24 15:03:52	8865	2.2 (3-σ u.l.)
794972027 (PC)	2017-12-25 02:19:28	2017-12-25 22:40:52	5432	1.2 ± 0.6
794972028 (PC)	2017-12-26 16:02:25	2017-12-26 21:05:53	5921	3.6 (3-σ u.l.)
794972029 (PC)	2017-12-27 14:23:32	2017-12-27 21:11:52	6231	3.3 (3-σ u.l.)
794972030 (PC)	2017-12-28 03:27:02	2017-12-28 08:01:52	2295	6.4 (3-σ u.l.)
794972031 (PC)	2017-12-29 14:11:03	2017-12-29 22:41:54	8453	2.8 (3-σ u.l.)
794972032 (PC)	2017-12-30 03:14:56	2017-12-30 19:28:53	9632	1.3 ± 0.5
794972033 (PC)	2017-12-31 00:03:15	2017-12-31 21:01:52	4028	4.5 (3-σ u.l.)
794972034 (PC)	2018-01-01 13:54:30	2018-01-01 23:47:53	9427	1.4 ± 0.6
794972035 (PC)	2018-01-02 09:15:27	2018-01-02 20:51:52	8788	3.0 (3-σ u.l.)
794972036 (PC)	2018-01-03 02:49:52	2018-01-03 14:19:54	9550	1.0 ± 0.5
794972037 (PC)	2018-01-04 10:46:59	2018-01-04 18:43:52	8231	1.0 ± 0.5
794972038 (PC)	2018-01-05 08:47:19	2018-01-05 18:57:53	9714	0.9 ± 0.4
794972039 (PC)	2018-01-08 08:30:33	2018-01-08 15:08:53	7557	3.1 (3-σ u.l.)
794972040 (PC)	2018-01-10 15:09:37	2018-01-10 20:05:54	4910	4.0 (3-σ u.l.)
794972041 (PC)	2018-01-12 09:56:31	2018-01-12 09:56:31	3753	5.1 (3-σ u.l.)
794972042 (PC)	2018-01-14 08:11:59	2018-01-14 14:48:54	4852	6.0 (3-σ u.l.)
794972043 (PC)	2018-01-16 04:54:20	2018-01-16 17:57:54	5256	4.0 (3-σ u.l.)
794972044 (PC)	2018-01-19 04:37:37	2018-01-20 09:28:52	4105	4.6 (3-σ u.l.)
794972045 (PC)	2018-02-21 04:36:37	2018-02-21 20:58:51	8490	5.0 (3-σ u.l.)

Notes. The columns show the identification number for each observation (ObsID, we omitted leading zeros), the T_{start} and T_{stop} times in TT, the exposure time, the average count rate (or the 3-σ upper limit when no statistically significant, above 2 σ, detection is made) in a source box-radius of 10 pixel centered on the source coordinates.

Table A.2. Log of the *Swift*/UVOT observations used in this work.

Tmid (s)	Terr (s)	AB Mag	Mag E+	Mag E-	AB MagU (3σ)	Rate (cts s^{-1})	Rate Err (cts s^{-1})	Flux (mJy)	Flux err (mJy)	Flux UL (3σ)	Filter	S/N
5000.13320	500.01330	20.075	+2.104	−0.671	18.694	1.3247e-01	1.1340e-01	0.03377	0.02891	0.12048	*V*	1.168
6111.27390	611.12740	18.554	+0.416	−0.300	17.827	5.3736e-01	1.7101e-01	0.13698	0.04359	0.26775	*V*	3.142
20371.95930	2037.19590	19.030	+0.305	−0.238	18.432	3.4678e-01	8.4968e-02	0.08840	0.02166	0.15337	*V*	4.081
24899.06130	2489.90610	18.725	+0.449	−0.316	17.964	4.5931e-01	1.5543e-01	0.11708	0.03962	0.23594	*V*	2.955
37194.89410	3719.48940	19.078	+1.998	−0.663	17.710	3.3182e-01	2.7914e-01	0.08458	0.07115	0.29805	*V*	1.189
45460.42610	4546.04260	18.997	+1.492	−0.606	17.720	3.5760e-01	2.6712e-01	0.09115	0.06809	0.29543	*V*	1.339
55562.74310	5556.27430	19.695	+nan	−0.798	18.122	1.8794e-01	2.0406e-01	0.04791	0.05202	0.20396	*V*	0.921
67910.01930	6791.00190	18.643	+0.612	−0.389	17.742	4.9503e-01	2.1336e-01	0.12619	0.05439	0.28935	*V*	2.320
83001.13470	8300.11350	19.589	+3.147	−0.722	18.130	2.0721e-01	1.9579e-01	0.05282	0.04991	0.20254	*V*	1.058
101445.83130	10144.58310	19.826	+2.556	−0.700	18.401	1.6662e-01	1.5079e-01	0.04247	0.03844	0.15778	*V*	1.105
123989.34940	12398.93490	19.171	+0.726	−0.431	18.193	3.0438e-01	1.4839e-01	0.07759	0.03783	0.19107	*V*	2.051
151542.53810	15154.25380	18.478	+0.587	−0.379	17.596	5.7671e-01	2.4074e-01	0.14701	0.06137	0.33111	*V*	2.396
185218.65770	18521.86580	18.722	+0.519	−0.350	17.896	4.6063e-01	1.7505e-01	0.11742	0.04462	0.25128	*V*	2.632
226378.35940	22637.83590	19.169	+0.366	−0.273	18.496	3.0519e-01	8.7246e-02	0.07780	0.02224	0.14451	*V*	3.498
276684.66150	27668.46610	20.010	+1.551	−0.614	18.720	1.4055e-01	1.0688e-01	0.03583	0.02724	0.11756	*V*	1.315
338170.14180	33817.01420	19.277	+0.455	−0.320	18.510	2.7614e-01	9.4483e-02	0.07039	0.02408	0.14264	*V*	2.923
617427.24110	61742.72410	18.195	+0.152	−0.133	17.836	7.4825e-01	9.7565e-02	0.19073	0.02487	0.26534	*V*	7.669
754633.29460	75463.32950	17.902	+0.124	−0.111	17.598	9.7991e-01	1.0543e-01	0.24978	0.0268	0.33041	*V*	9.294
922329.58230	92232.95820	17.722	+0.085	−0.079	17.500	1.1568e+00	8.7502e-02	0.29489	0.02230	0.36180	*V*	13.221
1127291.71170	112729.17120	17.773	+0.081	−0.075	17.561	1.1041e+00	7.8959e-02	0.28143	0.02013	0.34181	*V*	13.983
1377800.98100	137780.09810	17.799	+0.079	−0.074	17.591	1.0772e+00	7.5863e-02	0.27459	0.01934	0.33261	*V*	14.200
1683978.97680	168397.89770	18.411	+0.138	−0.123	18.078	6.1334e-01	7.3343e-02	0.15634	0.01870	0.21243	*V*	8.363
2058196.52720	205819.65270	18.626	+0.152	−0.133	18.268	5.0287e-01	6.5507e-02	0.12818	0.01670	0.17828	*V*	7.676
2515573.53320	251557.35330	19.156	+0.248	−0.202	18.637	3.0871e-01	6.3040e-02	0.07869	0.01607	0.12690	*V*	4.897
3074589.87390	307458.98740	20.848	+nan	−0.801	19.271	6.5006e-02	7.0919e-02	0.01657	0.01808	0.07080	*V*	0.917
3757832.06820	375783.20680	20.215	+1.081	−0.531	19.063	1.1638e-01	7.3368e-02	0.02966	0.01870	0.08577	*V*	1.586
4009.89170	400.98920	19.297	+0.265	−0.213	18.753	7.4653e-01	1.6183e-01	0.06881	0.01492	0.11356	*B*	4.613
5990.08510	599.00850	19.024	+0.233	−0.191	18.529	9.5987e-01	1.8513e-01	0.08848	0.01706	0.13967	*B*	5.185
24405.30400	2440.53040	18.855	+0.159	−0.138	18.484	1.1215e+00	1.5251e-01	0.10337	0.01406	0.14555	*B*	7.353
29828.70490	2982.87050	19.222	+0.159	−0.139	18.850	8.0004e-01	1.0909e-01	0.07374	0.01006	0.10391	*B*	7.334
36457.30590	3645.73060	18.831	+0.327	−0.251	18.205	1.1473e+00	2.9823e-01	0.10575	0.02749	0.18822	*B*	3.847
44558.92950	4455.89290	18.961	+0.369	−0.275	18.285	1.0177e+00	2.9314e-01	0.09380	0.02702	0.17486	*B*	3.472
54460.91380	5446.09140	18.917	+0.248	−0.202	18.398	1.0600e+00	2.1629e-01	0.09771	0.01994	0.15752	*B*	4.901
66563.33910	6656.33390	19.073	+0.241	−0.197	18.565	9.1803e-01	1.8253e-01	0.08462	0.01682	0.13509	*B*	5.029
81355.19220	8135.51920	18.826	+0.301	−0.235	18.233	1.1523e+00	2.7905e-01	0.10621	0.02572	0.18337	*B*	4.129
99434.12380	9943.41240	19.397	+0.383	−0.283	18.704	6.8127e-01	2.0271e-01	0.06280	0.01868	0.11885	*B*	3.361
121530.59580	12153.05960	19.719	+0.487	−0.335	18.921	5.0634e-01	1.8312e-01	0.04667	0.01688	0.09731	*B*	2.765
148537.39480	14853.73950	nan	+nan	−nan	19.610	-1.504e-01	2.3678e-01	−0.0139	0.02183	0.05161	*B*	−0.635

Notes. Columns 1 and 2 show the mid-time of each observations and the time binning divided by 2; Cols. 3–6 report the magnitude values in the AB system with positive and negative errors or a 3-σ upper limit in case of a non-detection; Cols. 7 and 8 show the count rates with errors, Cols. 9–11 the flux in mJy with errors and upper limits (in case of non-detections); Cols. 12 and 13 display the UVOT filter and the signal-to-noise ratio of the measure, respectively.

Table A.2. continued.

Tmid (s)	Terr (s)	AB Mag	Mag E+	Mag E-	AB MagU (3σ)	Rate (cts s^{-1})	Rate Err (cts s^{-1})	Flux (mJy)	Flux err (mJy)	Flux UL (3σ)	Filter	S/N
181545.70480	18154.57050	20.157	+1.017	−0.516	19.030	3.3826e-01	2.0569e-01	0.03118	0.01896	0.08806	*B*	1.644
221889.19480	22188.91950	20.025	+0.378	−0.280	19.339	3.8196e-01	1.1222e-01	0.03521	0.01034	0.06624	*B*	3.404
271197.90470	27119.79050	19.895	+0.378	−0.280	19.209	4.3049e-01	1.2652e-01	0.03968	0.01166	0.07467	*B*	3.403
331464.10580	33146.41060	19.900	+0.355	−0.267	19.240	4.2838e-01	1.1949e-01	0.03949	0.01101	0.07253	*B*	3.585
405122.79590	40512.27960	19.681	+2.190	−0.678	18.290	5.2436e-01	4.5462e-01	0.04833	0.04190	0.17404	*B*	1.153
605183.43590	60518.34360	19.320	+0.193	−0.164	18.887	7.3107e-01	1.1930e-01	0.06739	0.01100	0.10037	*B*	6.128
739668.64390	73966.86440	18.832	+0.115	−0.104	18.545	1.1463e+00	1.1548e-01	0.10566	0.01064	0.13759	*B*	9.926
904039.45360	90403.94540	18.686	+0.095	−0.088	18.442	1.3110e+00	1.1021e-01	0.12084	0.01016	0.15131	*B*	11.895
1104937.11000	110493.71100	18.769	+0.086	−0.080	18.545	1.2145e+00	9.2847e-02	0.11195	0.00856	0.13762	*B*	13.081
1350478.69000	135047.86900	19.069	+0.107	−0.098	18.799	9.2124e-01	8.6730e-02	0.08491	0.00799	0.10890	*B*	10.622
1650585.06550	165058.50660	19.482	+0.181	−0.155	19.070	6.2981e-01	9.6877e-02	0.05805	0.00893	0.08484	*B*	6.501
2017381.74670	201738.17470	19.913	+0.221	−0.184	19.434	4.2363e-01	7.8164e-02	0.03905	0.00720	0.06066	*B*	5.420
2465688.80160	246568.88020	20.497	+0.401	−0.292	19.785	2.4728e-01	7.6390e-02	0.02279	0.00704	0.04392	*B*	3.237
3013619.64630	301361.96460	20.597	+0.551	−0.364	19.744	2.2561e-01	8.9792e-02	0.02080	0.00828	0.04562	*B*	2.513
3683312.90110	368331.29010	21.274	+1.373	−0.587	20.027	1.2092e-01	8.6785e-02	0.01115	0.00800	0.03514	*B*	1.393
346.74660	34.67470	19.120	+0.272	−0.217	18.567	1.2471e+00	2.7593e-01	0.08196	0.01813	0.13636	*U*	4.520
5755.91820	575.59180	18.746	+0.109	−0.099	18.473	1.7604e+00	1.6745e-01	0.11570	0.01100	0.14871	*U*	10.513
15698.76520	1569.87650	18.776	+0.073	−0.068	18.583	1.7131e+00	1.1106e-01	0.11258	0.00730	0.13448	*U*	15.425
35032.10200	3503.21020	18.683	+0.124	−0.111	18.378	1.8660e+00	2.0152e-01	0.12263	0.01324	0.16236	*U*	9.260
42817.01360	4281.70140	19.174	+0.247	−0.201	18.656	1.1869e+00	2.4182e-01	0.07801	0.01589	0.12568	*U*	4.908
52331.90550	5233.19050	18.865	+0.141	−0.125	18.527	1.5774e+00	1.9190e-01	0.10367	0.01261	0.14150	*U*	8.220
63961.21780	6396.12180	19.005	+0.146	−0.128	18.658	1.3867e+00	1.7409e-01	0.09114	0.01144	0.12546	*U*	7.965
78174.82170	7817.48220	19.818	+0.300	−0.235	19.226	6.5565e-01	1.5846e-01	0.04309	0.01041	0.07433	*U*	4.138
95547.00430	9554.70040	19.607	+0.279	−0.222	19.043	7.9649e-01	1.8073e-01	0.05234	0.01188	0.08798	*U*	4.407
116779.67200	11677.96720	19.962	+0.295	−0.232	19.377	5.7443e-01	1.3654e-01	0.03775	0.00897	0.06467	*U*	4.207
142730.71020	14273.07100	20.637	+0.713	−0.427	19.667	3.0832e-01	1.4846e-01	0.02026	0.00976	0.04953	*U*	2.077
213215.01150	21321.50120	21.026	+0.452	−0.318	20.262	2.1553e-01	7.3424e-02	0.01416	0.00483	0.02864	*U*	2.935
260596.12520	26059.61250	20.563	+0.307	−0.239	19.963	3.3033e-01	8.1260e-02	0.02171	0.00534	0.03773	*U*	4.065
318506.37520	31850.63750	20.709	+0.408	−0.296	19.989	2.8867e-01	9.0482e-02	0.01897	0.00595	0.03681	*U*	3.190
389285.56970	38928.55700	21.431	+1.812	−0.645	20.091	1.4844e-01	1.2046e-01	0.00976	0.00792	0.03350	*U*	1.232
581525.35730	58152.53570	21.527	+1.127	−0.541	20.357	1.3588e-01	8.7740e-02	0.00893	0.00577	0.02623	*U*	1.549
710753.21440	71075.32140	21.198	+0.481	−0.332	20.405	1.8406e-01	6.5915e-02	0.01210	0.00433	0.02509	*U*	2.792
868698.37320	86869.83730	21.048	+0.452	−0.318	20.284	2.1116e-01	7.1963e-02	0.01388	0.00473	0.02807	*U*	2.934
1061742.45610	106174.24560	21.130	+0.375	−0.278	20.447	1.9588e-01	5.7186e-02	0.01287	0.00376	0.02415	*U*	3.425
1297685.22410	129768.52240	21.254	+0.422	−0.303	20.519	1.7475e-01	5.6332e-02	0.01148	0.00370	0.02259	*U*	3.102
1586059.71840	158605.97180	21.874	+0.920	−0.491	20.790	9.8677e-02	5.6375e-02	0.00648	0.00370	0.01760	*U*	1.750
1938517.43360	193851.74340	21.832	+0.782	−0.450	20.820	1.0257e-01	5.2663e-02	0.00674	0.00346	0.01712	*U*	1.948
2369299.08550	236929.90860	21.955	+0.885	−0.481	20.888	9.1584e-02	5.1052e-02	0.00602	0.00336	0.01608	*U*	1.794
2895809.99340	289580.99930	21.747	+0.715	−0.428	20.775	1.1100e-01	5.3564e-02	0.00729	0.00352	0.01786	*U*	2.072
3539323.32530	353932.33250	22.329	+2.665	−0.705	20.896	6.4951e-02	5.9371e-02	0.00427	0.00390	0.01597	*U*	1.094
4325839.61980	432583.96200	21.063	+0.715	−0.427	20.092	2.0826e-01	1.0046e-01	0.01369	0.00660	0.03349	*U*	2.073

Table A.2. continued.

Tmid (s)	Terr (s)	AB Mag	Mag E+	Mag E-	AB MagU (3σ)	Rate (cts s^{-1})	Rate Err (cts s^{-1})	Flux (mJy)	Flux err (mJy)	Flux UL (3σ)	Filter	S/N
5455.54780	545.55480	18.739	+0.108	−0.098	18.469	1.2140e+00	1.1468e-01	0.11570	0.01093	0.14849	$UVW1$	10.586
9960.67770	996.06780	18.654	+0.107	−0.097	18.385	1.3134e+00	1.2308e-01	0.12517	0.01173	0.16036	$UVW1$	10.671
14879.53090	1487.95310	18.819	+0.072	−0.067	18.628	1.1286e+00	7.2313e-02	0.10756	0.00689	0.12823	$UVW1$	15.607
33203.96470	3320.39650	19.109	+0.196	−0.166	18.672	8.6349e-01	1.4262e-01	0.08229	0.01359	0.12307	$UVW1$	6.055
40582.62350	4058.26230	19.830	+0.209	−0.175	19.371	4.4450e-01	7.7929e-02	0.04236	0.00743	0.06464	$UVW1$	5.704
49600.98420	4960.09840	19.617	+0.270	−0.216	19.067	5.4100e-01	1.1908e-01	0.05156	0.01135	0.08560	$UVW1$	4.543
60623.42520	6062.34250	20.376	+0.273	−0.218	19.821	2.6890e-01	5.9811e-02	0.02563	0.00570	0.04273	$UVW1$	4.496
74095.29740	7409.52970	20.658	+0.426	−0.305	19.920	2.0743e-01	6.7320e-02	0.01977	0.00642	0.03902	$UVW1$	3.081
90560.91910	9056.09190	20.841	+0.545	−0.361	19.993	1.7523e-01	6.9124e-02	0.01670	0.00659	0.03646	$UVW1$	2.535
110685.56780	11068.55680	22.052	+2.300	−0.685	20.650	5.7417e-02	5.0511e-02	0.00547	0.00481	0.01991	$UVW1$	1.137
135282.36060	13528.23610	21.137	+0.598	−0.383	20.247	1.3345e-01	5.6500e-02	0.01272	0.00538	0.02887	$UVW1$	2.362
202088.46460	20208.84650	21.826	+0.467	−0.325	21.048	7.0713e-02	2.4711e-02	0.00674	0.00236	0.01380	$UVW1$	2.862
246997.01230	24699.70120	21.966	+0.481	−0.332	21.174	6.2154e-02	2.2246e-02	0.00592	0.00212	0.01228	$UVW1$	2.794
301885.23730	30188.52370	nan	+nan	−nan	21.395	−1.5223e-02	4.0127e-02	−0.0015	0.00382	0.01002	$UVW1$	−0.379
368970.84560	36897.08460	22.406	+0.999	−0.511	21.286	4.1455e-02	2.4935e-02	0.00395	0.00238	0.01108	$UVW1$	1.663
551178.67050	55117.86710	22.547	+2.477	−0.696	21.128	3.6414e-02	3.2696e-02	0.00347	0.00312	0.01282	$UVW1$	1.114
673662.81950	67366.28200	23.329	+nan	−0.809	21.741	1.7724e-02	1.9600e-02	0.00169	0.00187	0.00729	$UVW1$	0.904
823365.66830	82336.56680	23.817	+nan	−1.138	21.775	1.1306e-02	2.0934e-02	0.00108	0.00200	0.00706	$UVW1$	0.540
1006335.81680	100633.58170	22.602	+0.754	−0.441	21.606	3.4614e-02	1.7336e-02	0.00330	0.00165	0.00826	$UVW1$	1.997
1229965.99840	122996.59980	23.093	+1.814	−0.645	21.753	2.2029e-02	1.7884e-02	0.00210	0.00170	0.00721	$UVW1$	1.232
1503291.77580	150329.17760	23.625	+nan	−0.874	21.943	1.3488e-02	1.6672e-02	0.00129	0.00159	0.00605	$UVW1$	0.809
1837356.61480	183735.66150	24.392	+nan	−1.338	22.097	6.6540e-03	1.6156e-02	0.00063	0.00154	0.00525	$UVW1$	0.412
2245658.08480	224565.80850	24.009	+nan	−1.070	22.058	9.4680e-03	1.5889e-02	0.00090	0.00151	0.00545	$UVW1$	0.596
2744693.21470	274469.32150	23.700	+nan	−0.899	21.981	1.2592e-02	1.6238e-02	0.00120	0.00155	0.00584	$UVW1$	0.775
3354625.04020	335462.50400	nan	+nan	−nan	22.180	−3.7920e-03	1.8277e-02	−0.0004	0.00174	0.00486	$UVW1$	−0.207
4100097.27140	410009.72710	24.259	+nan	−1.623	21.619	7.5220e-03	2.6020e-02	0.00072	0.00248	0.00816	$UVW1$	0.289
5227.53450	522.75350	18.871	+0.132	−0.117	18.551	7.3714e-01	8.4117e-02	0.10296	0.01175	0.13821	$UVM2$	8.763
9544.37370	954.43740	18.624	+0.074	−0.069	18.429	9.2513e-01	6.0966e-02	0.12922	0.00852	0.15477	$UVM2$	15.174
38886.48290	3888.64830	20.174	+0.323	−0.249	19.553	2.2194e-01	5.7087e-02	0.03100	0.00797	0.05492	$UVM2$	3.888
47527.92360	4752.79240	20.680	+0.324	−0.249	20.057	1.3929e-01	3.5970e-02	0.01946	0.00502	0.03453	$UVM2$	3.872
58089.68430	5808.96840	20.817	+0.616	−0.390	19.914	1.2276e-01	5.3130e-02	0.01715	0.00742	0.03941	$UVM2$	2.311
70998.50310	7099.85030	21.040	+0.490	−0.337	20.239	1.0001e-01	3.6342e-02	0.01397	0.00508	0.02920	$UVM2$	2.752
86775.94820	8677.59480	21.624	+0.697	−0.421	20.664	5.8392e-02	2.7658e-02	0.00816	0.00386	0.01975	$UVM2$	2.111
106059.49230	10605.94920	21.276	+0.458	−0.321	20.506	8.0470e-02	2.7706e-02	0.01124	0.00387	0.02285	$UVM2$	2.904
129628.26830	12962.82680	22.151	+0.954	−0.500	21.051	3.5958e-02	2.1017e-02	0.00502	0.00294	0.01383	$UVM2$	1.711
193642.22800	19364.22280	23.031	+1.506	−0.608	21.751	1.5983e-02	1.1990e-02	0.00223	0.00167	0.00726	$UVM2$	1.333
236673.83420	23667.38340	24.237	+nan	−1.151	22.179	5.2632e-03	9.9234e-03	0.00074	0.00139	0.00489	$UVM2$	0.530
289268.01960	28926.80200	22.215	+0.802	−0.456	21.192	3.3871e-02	1.7682e-02	0.00473	0.00247	0.01214	$UVM2$	1.916
353549.80180	35354.98020	23.198	+1.510	−0.608	21.917	1.3703e-02	1.0291e-02	0.00191	0.00144	0.00623	$UVM2$	1.332
645507.25120	64550.72510	26.843	+nan	−3.284	22.402	4.7730e-04	9.3522e-03	0.00007	0.00131	0.00399	$UVM2$	0.051
788953.30700	78895.33070	nan	+nan	−nan	22.367	−1.6660e-04	9.8760e-03	−0.0000	0.00138	0.00412	$UVM2$	−0.017
964276.26420	96427.62640	nan	+nan	−nan	22.970	−8.1047e-03	8.3352e-03	−0.0011	0.00116	0.00236	$UVM2$	−0.972
1178559.87840	117855.98780	nan	+nan	−nan	22.704	−3.5571e-03	8.3856e-03	−0.0005	0.00117	0.00302	$UVM2$	−0.424

Table A.2. continued.

Tmid (s)	Terr (s)	AB Mag	Mag E+	Mag E-	AB MagU (3σ)	Rate (cts s^{-1})	Rate Err (cts s^{-1})	Flux (mJy)	Flux err (mJy)	Flux UL (3σ)	Filter	S/N
1440462.07360	144046.20740	nan	+nan	−nan	22.730	−2.7624e-03	7.9510e-03	−0.0004	0.00111	0.00295	$UVM2$	−0.347
1760564.75670	176056.47570	nan	+nan	−nan	22.937	−6.4584e-03	7.9613e-03	−0.0009	0.00111	0.00243	$UVM2$	−0.811
2151801.36930	215180.13690	nan	+nan	−nan	22.691	−1.0908e-03	7.6468e-03	−0.0002	0.00107	0.00305	$UVM2$	−0.143
2629979.45130	262997.94510	nan	+nan	−nan	22.875	−4.2596e-03	7.5681e-03	−0.0006	0.00106	0.00258	$UVM2$	−0.563
3214419.32940	321441.93290	nan	+nan	−nan	23.263	−1.1364e-02	8.0921e-03	−0.0016	0.00113	0.00180	$UVM2$	−1.404
3928734.73590	392873.47360	nan	+nan	−nan	23.350	−1.5664e-02	9.1911e-03	−0.0022	0.00128	0.00166	$UVM2$	−1.704
4772.62190	477.26220	18.679	+0.108	−0.099	18.407	1.4872e+00	1.4124e-01	0.12241	0.01163	0.15729	$UVW2$	10.530
5833.20460	583.32050	18.685	+0.109	−0.099	18.410	1.4793e+00	1.4181e-01	0.12176	0.01167	0.15678	$UVW2$	10.431
19445.01410	1944.50140	19.341	+0.094	−0.087	19.100	8.0815e-01	6.7178e-02	0.06652	0.00553	0.08311	$UVW2$	12.030
29047.49010	2904.74900	20.249	+0.974	−0.505	19.140	3.5029e-01	2.0746e-01	0.02883	0.01708	0.08006	$UVW2$	1.688
35502.48790	3550.24880	21.276	+nan	−0.945	19.494	1.3602e-01	1.8869e-01	0.01120	0.01553	0.05779	$UVW2$	0.721
43391.92970	4339.19300	21.090	+0.365	−0.273	20.418	1.6149e-01	4.6084e-02	0.01329	0.00379	0.02467	$UVW2$	3.504
53034.58070	5303.45810	21.016	+0.353	−0.266	20.359	1.7279e-01	4.7935e-02	0.01422	0.00395	0.02606	$UVW2$	3.605
64820.04310	6482.00430	20.881	+0.349	−0.264	20.228	1.9564e-01	5.3775e-02	0.01610	0.00443	0.02938	$UVW2$	3.638
79224.49710	7922.44970	21.475	+0.319	−0.246	20.860	1.1321e-01	2.8794e-02	0.00932	0.00237	0.01643	$UVW2$	3.932
96829.94100	9682.99410	22.308	+0.815	−0.460	21.278	5.2556e-02	2.7751e-02	0.00433	0.00228	0.01118	$UVW2$	1.894
118347.70560	11834.77060	21.827	+0.328	−0.251	21.201	8.1848e-02	2.1317e-02	0.00674	0.00175	0.01200	$UVW2$	3.840
144647.19570	14464.71960	22.613	+1.164	−0.549	21.430	3.9694e-02	2.6110e-02	0.00327	0.00215	0.00971	$UVW2$	1.520
216077.90970	21607.79100	22.487	+0.488	−0.336	21.689	4.4575e-02	1.6143e-02	0.00367	0.00133	0.00766	$UVW2$	2.761
264095.22300	26409.52230	22.321	+0.439	−0.312	21.570	5.1938e-02	1.7287e-02	0.00428	0.00142	0.00854	$UVW2$	3.004
322783.05030	32278.30500	22.181	+0.417	−0.301	21.452	5.9123e-02	1.8862e-02	0.00487	0.00155	0.00952	$UVW2$	3.135
394512.61700	39451.26170	22.520	+1.362	−0.586	21.276	4.3258e-02	3.0922e-02	0.00356	0.00255	0.01120	$UVW2$	1.399
589333.66250	58933.36620	24.910	+nan	−1.572	22.329	4.7880e-03	1.5589e-02	0.00039	0.00128	0.00424	$UVW2$	0.307
720296.69860	72029.66990	23.776	+nan	−0.811	22.185	1.3602e-02	1.5102e-02	0.00112	0.00124	0.00485	$UVW2$	0.901
880362.63160	88036.26320	23.556	+2.878	−0.714	22.110	1.6650e-02	1.5474e-02	0.00137	0.00127	0.00519	$UVW2$	1.076
1075998.77190	107599.87720	23.587	+1.626	−0.624	22.282	1.6181e-02	1.2562e-02	0.00133	0.00103	0.00443	$UVW2$	1.288
1315109.61020	131510.96100	23.474	+1.240	−0.564	22.265	1.7972e-02	1.2235e-02	0.00148	0.00101	0.00450	$UVW2$	1.469
1607356.19020	160735.61900	24.002	+nan	−0.841	22.368	1.1042e-02	1.2909e-02	0.00091	0.00106	0.00410	$UVW2$	0.855
1964546.45470	196454.64550	25.797	+nan	−2.040	22.680	2.1150e-03	1.1736e-02	0.00017	0.00097	0.00307	$UVW2$	0.180
2401112.33350	240111.23330	23.777	+2.001	−0.663	22.410	1.3584e-02	1.1433e-02	0.00112	0.00094	0.00394	$UVW2$	1.188
2934692.85200	293469.28520	24.076	+nan	−0.859	22.415	1.0322e-02	1.2446e-02	0.00085	0.00102	0.00392	$UVW2$	0.829
3586846.81920	358684.68190	nan	+nan	−nan	22.850	−6.5630e-03	1.2830e-02	−0.0005	0.00106	0.00263	$UVW2$	−0.512
4383923.89010	438392.38900	23.881	+nan	−1.222	21.732	1.2344e-02	2.5684e-02	0.00102	0.00211	0.00736	$UVW2$	0.481